JOURNAL OF SPACECRAFT AND ROCKETS
Vol. 32, No. 5, September–October 1995

Low-Energy Neutral-Atom Imaging Techniques for Remote Observations of the Magnetosphere

Herbert O. Funsten[*] and David J. McComas[†]
Los Alamos National Laboratory, Los Alamos, New Mexico 87545
and
Earl E. Scime[‡]
West Virginia University, Morgantown, West Virginia 26506

Recent developments in the detection of neutral atoms will enable construction of space-based imagers that may reveal the global structure and dynamics of the terrestrial magnetosphere. The principal technical challenge of imaging low-energy neutral atoms having energies <30 keV is separating them from the intense uv background, to which their detectors are sensitive, with minimal loss of trajectory and energy information. Three instrument concepts for separating low-energy neutral atoms from the background uv are discussed: neutral-atom ionization via transmission through an ultrathin carbon foil and subsequent electrostatic deflection, uv grating polarizers and attenuators, and high-frequency shutters. Hardware associated with each of these concepts is mated to a detector section that provides trajectory, coincidence, and, if required, time-of-flight measurements.

Nomenclature

d = plate-set separation
E = low-energy neutral-atom (LENA) energy
E_0 = incident projectile (ion or LENA) energy
E_C = central energy loss of projectile through a foil
$E_{\rm FWHM}$ = full width at half maximum (FWHM) of energy-loss distribution
f = shutter oscillation frequency
k_F = foil constant
n = shutter oscillation period number
t = time
T_A = transmission through plate set
T_B = detector gating function
$T_{\rm LENA}$ = LENA detection function
v_C = central velocity of velocity passband
$v_{\rm FWFM}$ = full width at full maximum (FWFM) of velocity passband
$v_{\rm FWHM}$ = FWHM of velocity passband
v_M = maximum velocity of velocity passband
θ = relative polarization angle of two gratings
τ_P = shutter oscillation period
$\tau_{\rm TOF}$ = LENA time of flight between plate sets
ϕ = projectile angle of incidence
$\psi_{1/2}$ = scattering-half-width of projectile–foil interaction

Introduction

THIRTY years of single-point plasma, electric field, and magnetic field measurements have provided a statistically average picture of the terrestrial magnetosphere. Observations of the global dynamic nature of the magnetosphere have been limited by the lack of global coverage by satellites and the inability to measure beyond the local, microscopic spacecraft environment. An exciting new technique to image the global structure and dynamics of the magnetosphere is neutral-atom imaging.[1–4] This technique is based on magnetospheric emissions of hot plasma ions that have been neutralized by charge exchange with cold neutral atoms of the geocorona. Once these plasma ions are neutralized, they follow ballistic trajectories. If the trajectories of these neutral atoms can be detected remotely, then the source plasma can be imaged. Furthermore, these neutral atoms carry considerable information about the source plasma, including temperature, composition, and density.

Because of the different detection techniques required, neutral atoms have been partitioned into two energy regimes: energetic neutral atoms (ENAs, $E \geq 30$ keV) that primarily populate the ring current, and low-energy neutral atoms (LENAs, $E \leq 30$ keV) that populate the ring current, plasma sheet, and plasmasphere. Here, we focus on LENA imaging techniques.

The fundamental technical challenge of LENA imaging is separation of LENAs, whose fluxes are quite low,[5,6] from the intense uv background (predominantly H Ly-α), to which LENA detectors such as microchannel plates and channel electron multipliers are sensitive. ENA instruments typically utilize a thick foil through which ENAs pass with minimal angular scattering but uv cannot pass.[7,8] However, this technique is not feasible for LENA detection, since the thick foil greatly scatters and energy-straggles the LENAs and destroys their trajectory and energy information.

The first experiment to detect neutral atoms in space used a carbon foil to ionize the atoms and an electrostatic analyzer to deflect them into a detector.[9] Subsequent neutral-atom detectors utilized a slotted-disk velocity analyzer[10] and secondary ion emission.[11] Recent techniques proposed for LENA imaging include LENA charge modification (by either transmission through an ultrathin carbon foil[3,12,13] or reflection from a low work function surface[14–16]) with subsequent electrostatic deflection and direct uv blocking using free-standing gratings.[17,18]

In this paper, we focus on the three techniques illustrated in Fig. 1 for separating LENAs from the uv background. The first, which is technologically mature, involves LENA charge conversion by transmission through an ultrathin carbon foil and subsequent electrostatic deflection. The other two concepts, which are developing technologies, utilize uv grating polarizer–attenuators and high-frequency shutters. Laboratory results are presented for each concept.

In a LENA imager, a different front end of the instrument is used for each of these concepts, and a similar detector section, to which the front end is mated, can be used for all three cases. The measurement capabilities of the detector section typically include LENA trajectory measurement for imaging, coincidence for high-signal-to-background measurements, and time of flight for velocity measurements.

Presented as Paper 95-0618 at the AIAA 33rd Aerospace Sciences Meeting and Exhibit, Reno, NV, Jan. 9–12, 1995; received Jan. 31, 1995; revision received April 28, 1995; accepted for publication May 3, 1995.

[*] Technical Staff Member, Space and Atmospheric Sciences Group. Member AIAA.

[†] Group Leader, Space and Atmospheric Sciences Group.

[‡] Assistant Professor, Department of Physics.

LENA Charge Modification by an Ultrathin Foil

A basic foil-based LENA imager, illustrated in Fig. 1a, is designed for a spinning spacecraft.[12] LENAs transit a collimator (which consists of serrated and blackened plates that are alternately biased to reject ambient plasma ions) that sets the azimuthal field of view. LENAs then pass through an ultrathin (1.1-μg cm^2) carbon foil that is supported by a fine, high-transmission grid. A fraction of these LENAs are ionized, according to the data[6] shown in Fig. 2. The ionized LENAs then enter an electrostatic analyzer (ESA), e.g., a hemispherical ESA as shown in Fig. 1a, and can pass through to the detector if their energy is within the ESA energy passband.

One possible detector section configuration, which is illustrated in Fig. 1a for a foil-based imager, consists of a second ultrathin carbon foil and separate LENA and electron detectors. A LENA transits the second foil, induces secondary electron (SE) emission, and is detected at the position-sensitive LENA detector. SEs, which provide the location at which the LENA transited the foil, are steered toward and detected at the position-sensitive electron detector. The LENA and SE position measurements are used to calculate the incident polar trajectory of the LENA. Furthermore, detection of both a LENA and its associated SEs is used for a coincidence measurement to reject noise counts created spuriously or by penetrating radiation. This scheme can also be employed as a time-of-flight measurement to determine the LENA mass.

One important issue is maintaining the incident LENA trajectory and energy information throughout the instrument. The interactions between a LENA and the carbon foils result in both angular scattering, which acts to degrade the image resolution, and energy straggling, which is a loss of energy information. We have performed laboratory experiments to examine each of these effects.

The results of scattering experiments of H, He, and O transiting 1.1-μg cm^{-2} carbon foils are shown in Fig. 3.[16] Angular scattering can be quantified by $E_0\psi_{1/2} = k_F$, where E_0 is the incident LENA energy, $\psi_{1/2}$ is the angular scattering halfwidth, and k_F is a constant that depends on the LENA species, foil thickness, and foil composition. This representation, shown as the solid lines in Fig. 3, yields $k_F = 12.6$ for H, $k_F = 34$ for He, and $k_F = 133$ for O for the foils used here. The apparent deviation of the H data from the solid line for $\psi_{1/2} < 1$ deg is an artifact arising from the finite aperture width in the experimental apparatus. Comparison of the H scattering data with semiempirical scattering theory[19] (assuming the foil is composed of carbon only) indicates that the foil thickness is $\approx$1.1 μg cm^{-2} which is slightly more than twice the nominal value of 0.5 μg cm^{-2} quoted by the manufacturer. At lower energies, $\psi_{1/2}$ increases and the polar resolution gradually degrades, although the azimuthal resolution that is set by the collimator is fully retained.

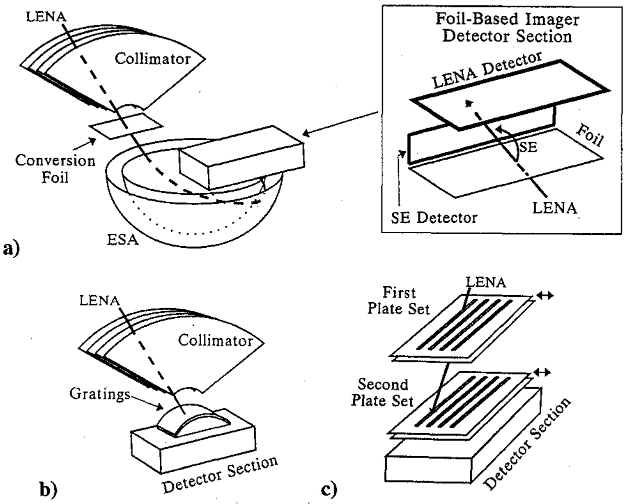

Fig. 1 LENA imager schematics for a) foil-based instrument with its detector section, b) grating-based imager, and c) high-frequency shutter-based imager.

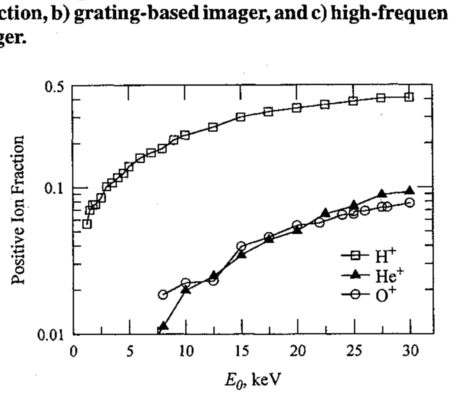

Fig. 2 Experimental data showing the probability that H, He, and O exits a 1.1-μg cm^{-2} carbon foil as a positive ion. The solid lines are to guide the eye.

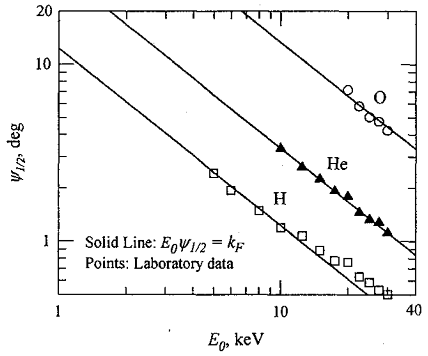

Fig. 3 Angular scattering of H, He, and O that transit a 1.1-μg cm^{-2} carbon foil.

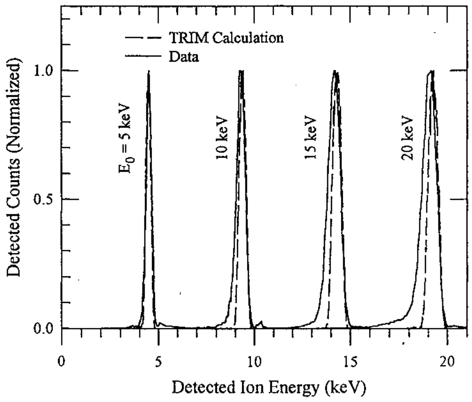

Fig. 4 Energy spectra of incident 5-, 10-, 15-, and 20-keV H$^+$ that transit a 1.1-μg cm^{-2} carbon foil.

Since the LENA energy distribution also provides insight into the properties of the source plasma, energy loss of LENAs through the first foil may degrade the energy information that is measured using the ESA. A laboratory experiment to examine the energy loss of H and He that transit an ultrathin foil consisted of passing a monoenergetic ion beam through a foil and measuring the energies of singly positive ions emerging from the foil using a voltage-scanned electrostatic energy analyzer followed by a channel electron-multiplier detector. Since the mean free path of charge exchange of a projectile in a foil is much less than the foil thickness, these results are independent of both the incident and the exit charge states of the projectile. The results are shown in Fig. 4 (solid lines) for incident H$^+$ at energies of 5, 10, 15, and 20 keV. The dashed lines, which are the results of the transport of ions in matter (TRIM) computer code,[20] show excellent agreement with the data at lower energies, but indicate slightly less energy loss at higher E_0.

To characterize the energy loss, we define the central energy E_C as the energy corresponding to the maximum of the exit energy distribution, and we examine the variation between E_C and E_0 using the ratio $(E_0 - E_C)/E_0$. In Fig. 5a, the data for H show that $(E_0 - E_C)/E_0$ decreases with increasing energy from 10% at E_0 = 5 keV to 4.8% at E_0 = 20 keV. The values are slightly higher for He than for H.

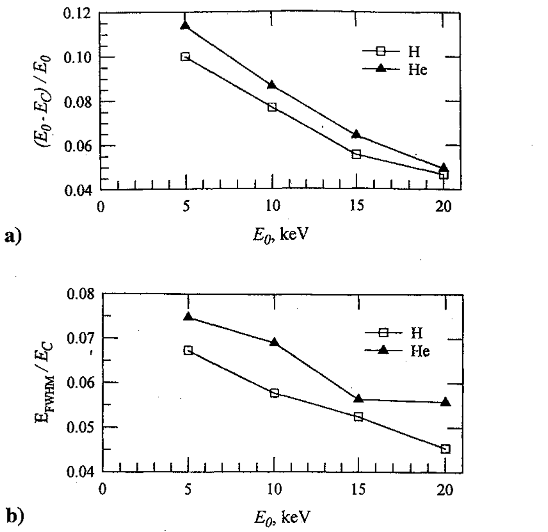

Fig. 5 Energy-loss statistics of H^+ and He^+ transiting a 1.1-μg cm^{-2} carbon foil: a) central energy E_C relative to incident energy E_0 and b) full width at half maximum relative to E_C.

The FWHM of the energy distribution, E_{FWHM}, normalized to E_C, is shown in Fig. 5b. This ratio for H decreases from 6.7% at $E_0 = 5$ keV to 4.5% at 20 keV, and the ratio for He is approximately 1% higher than for H. Since the energy passband of a electrostatic analyzer in a foil-based instrument is typically large (for example, 25%) relative to both the energy loss and width of the energy-loss distributions, the energy characterization of LENAs is not significantly degraded by the foil.

The geometric factor of this type of instrument ranges from 0.05 to 1 sr cm^2 keV/keV depending on the spacecraft resources available, and the targeted energy range is 0.8–30 keV. The field of view is 120 deg (azimuthal) × 2 deg (polar) instantaneous, and 120 deg × 360 deg over one spacecraft spin, with a nominal pixel resolution of 2 deg × 2 deg FWHM. Based on these parameters, the LENA pixel count rate would range from a few to hundreds of counts per second, depending on the dynamic state of the magnetosphere.[5,6]

UV Blocking via Freestanding Grating Nanostructures

The second concept for separating LENAs from the background uv involves direct blocking of the uv using freestanding gold gratings mounted on a support structure having 35–45% transmission.[18,21] As shown in Fig. 1b, a suite of gratings is located between a collimator that sweeps out ambient ions and electrons and a detector section that measures LENA trajectories and, using time of flight, LENA velocities.

The gratings consist of regularly spaced solid bars and open slits through which LENAs can pass. To block uv efficiently, these gratings, which act as both polarizers and waveguides, must have a slit width comparable to or less than the uv wavelength, predominantly 121.6 nm (H Ly-α). The gratings investigated here were fabricated using holographic lithography and were determined by scanning electron microscope (SEM) measurements to have typically a 200-nm period, 5200-nm thickness, and a 100–140-nm, bar width, resulting in a 100–60-nm slit width, respectively.

Three experiments were performed to characterize the gratings. First, the atomic transmission through the gratings was measured by directing a 10-keV H^+ beam onto a microchannel plate detector and measuring the count rate with and without the grating located directly in front of the detector. Note that transmission of atomic projectiles through the grating should be independent of the charge state, and quantum effects of LENA transmission can be ignored since the atomic DeBroglie wavelength is $<10^{-2}$ nm for H energies >10 eV. The measured transmission of H^+ at normal incidence ranged from 8 to 15%, in agreement the SEM measurements. Figure 6 shows the variation of H^+ transmission as a function of the azimuthal angle of incidence ϕ defined as shown in the figure. For the geometry shown in Fig. 6, the calculated transmission as a function of the angle of incidence is depicted as the solid line and agrees well with the data. The data indicate that the angular half-width of the transmission in the direction of ϕ equals ≈4.5 deg.

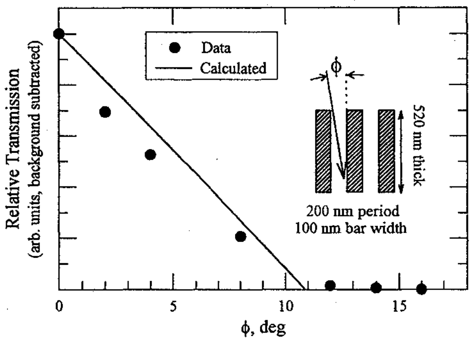

Fig. 6 Ion transmission through a grating as a function of incident azimuthal angle ϕ. The solid line represents the calculated transmission based on the illustrated grating geometry.

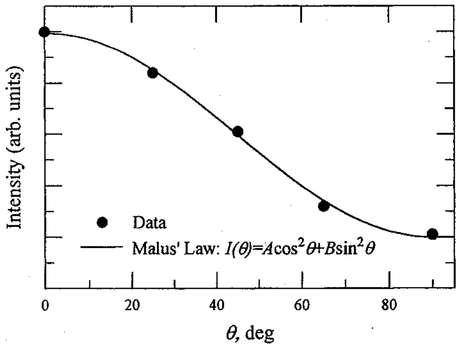

Fig. 7 UV transmission through two crossed gratings as a function of relative polarization angle θ.

The second experiment involved measuring the transmission of unpolarized uv from a deuterium lamp through two gratings as a function of the angle θ between their polarization axes. The data are shown in Fig. 7 along with a fit to the data according to Malus' law.[21] As θ increases from 0 deg (polarization axes parallel) to 90 deg (polarization axes perpendicular), the transmission decreases to a small, but nonzero, value. These results indicate that although the polarization attenuation of each grating is nearly one order of magnitude, the gratings do not act as ideal polarizers, since the uv transmission does not decrease to zero when $\theta = 90$ deg.

The third experiment measured the absolute transmission of unpolarized uv through a single grating by comparing the results with a calibrated uv filter having a transmission of 10^{-4}. The uv transmission through a single perfect grating polarizer should be the product of the polarization effect (0.5) and the grating transparency (≈0.1 for our gratings), yielding a net transmission of ≈0.05. However, the measured uv transmission through the grating was 4×10^{-4}, which is significantly less than can be explained by the polarization effect alone. Examination of the transmission physics indicates that the waveguide effect, in which the grating resistively dissipates the uv passing through the slits, is responsible for the bulk of the uv attenuation in the grating.[21]

For example, using two crossed gratings, the uv transmission can be reduced by approximately 10^{-7}, which, in conjunction with the LENA coincidence detection scheme and a low quantum detection efficiency of uv by microchannel plates, is sufficient to suppress a uv flux of $\sim 10^{10}$ cm^{-2} s^{-1} reflected from the geocorona. A crossed grating set results in a LENA transmission of at least 1% with no degradation of the incident trajectory or energy. Since a crossed grating set has a polar field of view of ≈9 deg FWHM as shown in Fig. 6, several crossed grating sets could be affixed in a semicircle directly in front of the detector section to accommodate a wide field of view. Time-of-flight measurements in conjunction with species-dependent pulse-height information[22] from the LENA detector would be used to estimate the LENA species and energy.

UV Trapping via High-Frequency Shutters

A third method of separating LENAs from background uv acts as a light trap similar to the slotted-disk velocity analyzer, from which some of the first measurements of neutral-atom fluxes in space were obtained.[10] Rotating-disk instruments are impractical for most spacecraft, since they require exceedingly large spacecraft resources (especially mass and power), induce severe torque on the spacecraft, and have limited operational lifetimes.

We have investigated high-frequency shutter techniques, illustrated in Figs. 1c and 8, that have a long lifetime and consume minimal spacecraft resources. In Fig. 8a, the technique involves two sets of plates separated by a distance d, with each set having one moving plate and one stationary plate. Each plate has an aperture whose width is less than half the travel of the moving plate. The moving plates are mounted on, for example, ceramic piezoelectric crystals that are driven by a tunable oscillator. In conjunction with resonance vibration frequencies of the mounting bracket to which the plates are attached, total plate motions of 1 mm are possible. Typical oscillation frequencies range from 0.5 to 5 kHz.

We have performed preliminary laboratory experiments to examine the feasibility of a shutter-based LENA imager. The apparatus consisted of an aluminum plate, suspended by fine wires, that was driven into oscillation at its natural frequency for the lowest-order bending mode by means of high-frequency electromagnetic coupling. The experiment was designed to verify the theoretically predicted natural frequency of the plate. Although acoustically damped, the end of the plate was observed to oscillate a few tens of micrometers at a frequency of a few kilohertz. In vacuum the travel of the end of the plate should move a lightweight slit plate nearly to 1 mm, which is sufficient for the shutter-based imaging technique.

The oscillating plates are 180 deg out of phase, and uv trapping proceeds as shown in Fig. 8a for one-half of an oscillation period. The apertures of the first plate set are initially aligned so that neutral atoms can enter the region between the plates. Ultraviolet light also can enter, but the apertures of the second plate set are misaligned, so the uv cannot enter the detector section. As time proceeds, both plate sets become misaligned, and the region between the plate sets acts as a light trap in which the uv is absorbed. Finally, while the first plate set is misaligned so that uv is blocked, the second plate set becomes aligned so that neutral atoms can enter the detector section. The moving plates then reverse direction to complete the oscillation cycle.

The technique illustrated in Fig. 8b is similar to that described in Fig. 8a except the second plate set is replaced with a detector that is electrically gated to operate only when the apertures of the first plate set are misaligned, resulting in rejection of uv.

To examine in detail the LENA transmission through a shutter-based imager, we use an imager consisting of one plate set and a gated detector as in Fig. 8b. The transmission $T_A(t)$ of LENAs through the plate set, which has one rectangular aperture on each plate, can be represented as a triangular-shaped function depicted in the top panel of Fig. 9a that is dependent on the elapsed time t normalized to the oscillation period τ_P. Within the first oscillation period, the apertures of the plate set are partially or fully aligned from $t = 0$ to $t = \tau_1$ and are misaligned for all other times. This transmission function can be represented for all oscillation periods as

$$T_A(t) = \begin{cases} 2(t - n\tau_P)/\tau_1 & \text{for} \quad 0 \le t - n\tau_P \le \tau_1/2 \\ 2 - 2(t - n\tau_P)/\tau_1 & \text{for} \quad \tau_1/2 \le t - n\tau_P \le \tau_1 \\ 0 & \text{otherwise} \end{cases} \tag{1}$$

where $n = 0, 1, 2, \ldots$.

The gating function $T_B(t)$, which describes the time that the detector is activated, is a boxcar function as illustrated in the bottom panel of Fig. 9a. Within one oscillation period, the detector is on only during the time from $t = \tau_2$ to $t = \tau_3$. For a detector gated with period τ_P, the gating function is

$$T_B(t) = \begin{cases} 1 & \text{for} \quad \tau_2 \le t - n\tau_P \le \tau_3 \\ 0 & \text{otherwise} \end{cases} \tag{2}$$

where $n = 0, 1, 2, \ldots$. The time interval $\tau_2 - \tau_1$ must be set long enough so that uv is absorbed and photoelectrons are electrostatically removed before the detector is turned on.

We immediately see that LENAs with a certain time of flight t_{TOF} between the plate set and the detector can be detected. Furthermore, LENAs that pass through the plate set during the first oscillation (i.e., during $0 < t < \tau_1$) can be detected during the same or any subsequent gating period. Therefore, the detection function representing LENAs that pass through the plate set and are detected is

$$T_{\mathrm{LENA}}(t_{\mathrm{TOF}}) = \int_0^{\tau_1} T_A(t) T_B(t + t_{\mathrm{TOF}})\,\mathrm{d}t \tag{3}$$

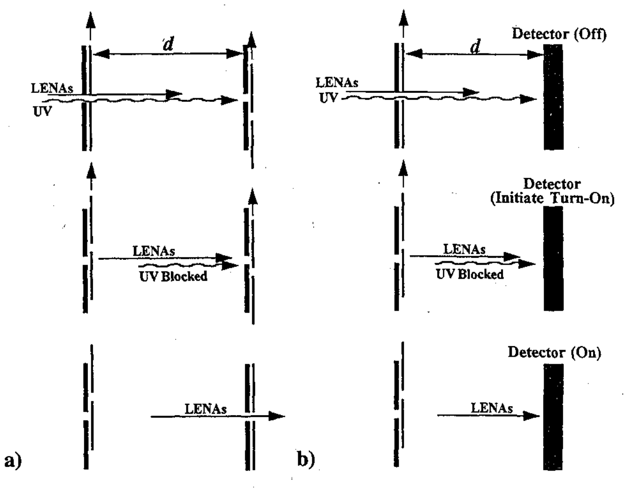

Fig. 8 Two possible LENA detection schemes using high-frequency shutters: a) two plate sets, each set having one oscillating plate, and b) single plate set with a gated detector.

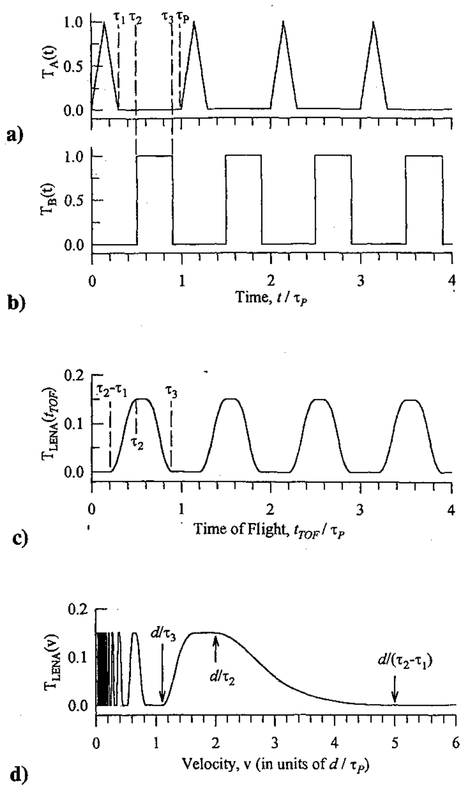

Fig. 9 Construction of the velocity passbands of a LENA imager using a single plate set and gated detector: a) transmission function T_A of the plate set; b) gating function T_B of the detector; c) characteristic LENA time-of-flight passbands for the imager, derived using Eq. (3); and d) the corresponding velocity passbands for the imager.

Table 1 **High-frequency shutter transmission characteristics of the *n*th velocity passband**

Quantity	Governing equation ($n = 0, 1, 2, \ldots$)
Passband spacing	$\sim[(n+1)\tau_P + \text{constant}]^{-1}$
Max. velocity	$v_{\max} = d/(n\tau_P + \tau_2 - \tau_1)$
FWHM velocity	$v_{\text{FWHM}} = d/(n\tau_P + \tau_3 - \tau_2)$
FWFM velocity	$v_{\text{FWFM}} = d/(n\tau_P + \tau_3 - \tau_2 + \tau_1)$
Central velocity	$v_C = df/(n + \Delta\tau/\tau_P)$

This is shown in Fig. 9b for the transmission function $T_A(t)$ and gating function $T_B(t)$ depicted in Fig. 9a. The resulting time-of-flight (TOF) passbands have a period equal to τ_P, and the minimum TOF for passage of a LENA through both plate sets equals $\tau_2 - \tau_1$. Other characteristic times of $T_{\text{LENA}}(t_{\text{TOF}})$ are illustrated in Fig. 9b.

The TOF passbands are easily converted into velocity passbands using the relationship $v = d/t_{\text{TOF}}$, where v is the velocity component normal to the detector surface. The resulting velocity-dependent detection function $T_{\text{LENA}}(v)$ is shown in Fig. 9c. Some important properties of the nth velocity passband are listed in Table 1, where we define the central TOF of the first TOF passband as $\Delta\tau = (\tau_2 + \tau_3 - \tau_1)/2$ and the plate oscillation frequency as $f = \tau_P^{-1}$. Note that v_C is proportional to both f and d. If $T_A(t)$ and $T_B(t)$ are 180 deg out of phase, then $\Delta\tau \approx 0.5\tau_P$ and we obtain a simple equation for the central velocity of the highest ($n = 0$) velocity passband, $v_C \approx 2df$.

The numerous velocity passbands can make a particular velocity measurement somewhat ambiguous. However, this problem might be solved by pseudorandom oscillations of the moving plate or by dynamically varying the velocity passbands by adjusting τ_P and $\Delta\tau$.

We note that the above analysis is quite general, and numerous variations of the basic technique might be employed. For example, to attain higher energies, several smaller equally spaced apertures could be located on each plate in the direction of oscillation of the moving plates, so that one complete oscillation of the moving plates produced more than one transmission period. This would act to increase the maximum detectable LENA velocity by a factor equal to the number of apertures. For example, if $f = 5$ kHz, $d = 30$ cm, and 20 apertures were placed along the direction of oscillation, then $v_C \approx 6 \times 10^6$ cm/s, which corresponds to 19-eV H, 75-eV He, and 300-eV O. Furthermore, if $v_{\max} \approx 2.5v_C$ as shown in Fig. 9c, then the maximum energy observable is 119 eV for H, 469 eV for He, and 1.9 keV for O.

The geometry of the plates provides an intrinsic collimation, and electrostatic fields within the region between the plate sets could be utilized to sweep out ambient plasma ions and electrons in addition to photoelectrons. Since this type of instrument has an intrinsic velocity passband and LENA trajectories are not altered in any way, it would be particularly suitable for imaging very low-energy neutral atoms, for example, heliospheric neutral atoms.[14]

Discussion and Summary

Three viable concepts for LENA imaging have been presented. The first, involving charge conversion of LENAs using an ultrathin foil and subsequent electrostatic deflection away from the uv, is technologically mature. The other two concepts, direct uv blocking with freestanding gratings and uv trapping using high-frequency shuttering, are developing technologies that should provide imaging over a wider energy range with less demand on spacecraft resources.

Each of these concepts has unique advantages. The foil-based method provides a direct energy measurement of LENAs, yielding the LENA mass when used with a time-of-flight detector scheme. This imager has a practical energy range of 0.8 to 30 keV, within which a majority of the magnetospheric LENA flux resides.

Separation of LENAs from the uv in the grating-based imager does not alter the LENA trajectory in any way and is superior for imaging at LENA energies <1 keV. Furthermore, the energy passband is infinite, which acts to increase the geometric factor. LENA velocity and mass determination can be obtained using time-of-flight measurements in conjunction with pulse-height analysis. This type of instrument does not have an electrostatic analyzer and therefore requires less in the way of spacecraft resources.

Like the grating-based imager, separation of LENAs from the uv in the shutter-based imagers does not alter the LENA trajectory. The shutter-based imager has numerous but clearly defined velocity passbands. Ideally, this type of instrument can be utilized for imaging LENAs with energies up to a few keV and can provide a mass estimate when used in conjunction with species-dependent pulse-height distributions derived from the LENA detector. This technology is currently under development and promises an interesting velocity-filtered approach to neutral-atom imaging.

The bulk of the LENA fluxes is anticipated to be within an energy range of several hundred electron volts to tens of keV. The three concepts presented here should enable unique imaging capabilities within and beyond this energy range to image the global structure and dynamics of the terrestrial magnetosphere. These unprecedented measurements could potentially provide revolutionary insight into fundamental aspects of the magnetosphere by directly observing, for example, the plasma sheet; magnetic reconnection in the tail region; the ring current variation in composition, energy, and density during substorms and storms; plasma injection from the tail; and auroral upflows.

Acknowledgments

This work was performed under the auspices of the United States Department of Energy. The authors wish to thank J. Baldonado and D. Everett for laboratory assistance and A. Migliori for development of the shutter-based laboratory experiment.

References

[1] Roelof, E. C., Mitchell, D. G., and Williams, D. J., "Energetic Neutral Atoms ($E \sim 50$ keV) from the Ring Current: IMP 7/8 and ISEE 1," *Journal of Geophysical Research*, Vol. 90, No. A11, 1985, pp. 10,991–11,008.

[2] Roelof, E. C., "Energetic Neutral Atom Image of a Storm-Time Ring Current," *Geophysical Research Letters*, Vol. 14, No. 6, 1987, pp. 652–655.

[3] McComas, D. J., Barraclough, B. L., Elphic, R. C., Funsten, H. O., and Thomsen, M. F., "Magnetospheric Imaging with Low-Energy Neutral Atoms," *Proceedings of the National Academy of Sciences of the United States of America*, Vol. 88, No. 14, 1991, pp. 9598–9602.

[4] Williams, D. J., Roeloff, E. C., and Mitchell, D. G., "Global Magnetospheric Imaging," *Reviews of Geophysics*, Vol. 30, No. 3, 1992, pp. 183–208.

[5] Moore, K. R., Scime, E. E., Funsten, H. O., McComas, D. J., and Thomsen, M. F., "Low Energy Neutral Atom Emission from the Earth's Magnetosphere," *Optical Engineering*, Vol. 33, No. 2, 1994, pp. 342–348.

[6] Funsten, H. O., McComas, D. J., Moore, K. R., Scime, E. E., and Thomsen, M. F., "Imaging of Magnetospheric Dynamics Using Low Energy Neutral Atom Detection," *Solar System Plasma Physics: Resolution Processes in Space and Time*, edited by J. L. Burch and J. H. Waite, Vol. 84, Geophysical Monograph Series, American Geophysical Union, Washington, DC, 1994, pp. 275–282.

[7] McEntire, R. W., and Mitchell, D. G., "Instrumentation for Global Magnetospheric Imaging via Energetic Neutral Atoms," *Solar System Plasma Physics*, edited by J. H. Waite, J. L. Burch, and R. L. Moore, Vol. 54, Geophysical Monograph Series, American Geophysical Union, Washington, DC, 1989, pp. 69–80.

[8] Hsieh, K. C., and Curtis, C. C., "Remote Sensing of Planetary Magnetospheres: Mass and Energy Analysis of Energetic Neutral Atoms," *Solar System Plasma Physics*, edited by J. H. Waite, J. L. Burch, and R. L. Moore, Vol. 54, Geophysical Monograph Series, American Geophysical Union, Washington, DC, 1989, pp. 159–164.

[9] Bernstein, W., Wax, R. L., Sanders, N. L., and Inouye, G. T., "An Energy Spectrometer for Energetic (1–25 keV) Neutral Hydrogen Atoms," *Small Rocket Instrumentation Techniques*, edited by K.-I. Maeda, North-Holland, Amsterdam, 1969, pp. 224–231.

[10] Moore, J. H., and Opal, C. B., "A Slotted Disk Velocity Analyzer for the Detection of Energetic Atoms Above the Atmosphere," *Space Science and Instrumentation*, Vol. 1, No. 1, 1975, pp. 377–386.

[11] Rosenbauer, H., Fahr, H. J., Keppler, E., Witte, M., Hemmerich, P., Lauche, H., Loidl, A., and Zwick, R., "The ISPM Interstellar Neutral Gas Experiment," *The International Solar Polar Mission— Its Scientific Investigations*, edited by K. P. Wenzel, R. G. Marsden, and B. Battrick, SP-1050, European Space Agency, 1983, pp. 125–139.

[12] McComas, D. J., Funsten, H. O., Gosling, J. T., Moore, K. R., Scime, E. E., and Thomsen, M. F., "Fundamentals of Low Energy Neutral Atom Imaging," *Optical Engineering*, Vol. 33, No. 2, 1994, pp. 335–341.

[13] Funsten, H. O., McComas, D. J., and Barraclough, B. L., "Ultrathin Foils Used for Low Energy Neutral Atom Imaging of Planetary Magnetospheres," *Optical Engineering*, Vol. 32, No. 12, 1993, pp. 3090–3095.

[14]Gruntman, M. A., "A New Technique for in Situ Measurement of the Composition of Neutral Gas in Interplanetary Space," *Planetary and Space Science*, Vol. 41, No. 4, 1993, pp. 307–319.

[15]Ghielmetti, A. G., Shelly, E. G., Fuselier, S. A., Wurz, P., Boschler, P., Herrero, F. A., Smith, M. F., and Stephen, T. S., "Mass Spectrograph for Imaging Low-Energy Neutral Atoms," *Optical Engineering*, Vol. 33, No. 2, 1994, pp. 362–370.

[16]Funsten, H. O., McComas, D. J., and Scime, E. E., "Comparative Study of Low Energy Neutral Atom Imaging Techniques," *Optical Engineering*, Vol. 33, No. 2, 1994, pp. 349–356.

[17]Scime, E. E., Funsten, H. O., Gruntman, M. A., McComas, D. J., and Moore, K. R., "A Novel Low Energy Neutral Atom Imaging Technique," *Optical Engineering*, Vol. 33, No. 2, 1994, pp. 357–361.

[18]Gruntman, M. A., "Submicron Structures—Promising Filters in EUV: A Review," *Proceedings of SPIE*, Vol. 1549, July 1991, pp. 385–394.

[19]Meyer, L., "Plural and Multiple Scattering of Low-Energy Heavy Particles in Solids," *Physica Status Solidi B*, Vol. B44, No. 1, 1971, pp. 253–268.

[20]Ziegler, J. F., Biersack, J. P., and Littemark, U., "Transport of Ions in Matter (TRIM) Computer Code," *The Stopping and Range of Ions in Solids*, 1st ed., Vol. 1, Pergamon, New York, 1985, pp. 202–263.

[21]Scime, E. E., Anderson, E. H., McComas, D. J., and Schattenburg, M. L., "Extreme Ultraviolet Polarization and Filtering with Gold Transmission Gratings," *Applied Optics*, Vol. 34, No. 4, 1995, pp. 648–654.

[22]Mitchell, D. G., Cheng, A. F., Krimigis, S. M., Keath, E. P., Jaskulek, S. E., Mauk, B. H., McEntire, R. W., Roelof, E. C., Williams, D. J., Hsieh, K. C., and Drake, V. A., "INCA: The Ion Neutral Camera for Energetic Neutral Atom Imaging of the Saturnian Magnetosphere," *Optical Engineering*, Vol. 32, No. 12, 1993, pp. 3096–3101.

A. L. Vampola
Associate Editor